High-Speed X-Ray Imaging of Droplet-Powder Interaction in Binder Jet Additive Manufacturing

Jacob E. Lawrence¹, Madi P. Lawrence¹, Kamel Fezzaa², Samuel J. Clark², Nathan B. Crane¹

¹Department of Mechanical Engineering, Brigham Young University, Provo, UT, 84602, USA ²X-ray Science Division, Advanced Photon Source, Argonne National Laboratory, Argonne, IL, 60439, USA

Keywords:

- Binder Jetting
- Inkjet
- Synchrotron X-ray Imaging
- Binder-Powder Interaction
- SS316L

Abstract

Binder jetting (BJ) is an additive manufacturing process that uses a powder feedstock in a layer wise process to print parts by selectively depositing a liquid binder into the powder bed using inkjet technology. This study presents findings from high-speed synchrotron imaging of binder droplet-interaction during the BJ printing process. A custom laboratory-scale BJ test platform was used for testing which enabled control of relevant process parameters including powder material, print geometry, spacing between droplets, powder bed density, and powder moisture content. Powder ejection was observed above the powder bed surface and powder relocation due to droplet impact was observed below the powder bed surface. Powder relocation was observed to be sensitive to powder material, powder bed density, powder bed moisture, droplet spacing, and print geometry. Increasing powder bed density was found to increase particle ejection velocity but reduce the total number of particles ejected. Process parameters that increase binder / moisture content in the powder bed were found to reduce powder ejection. The number of ejected powder particles was reduced for lower droplet spacings. Both powder ejection and powder relocation below the powder bed were reduced by treating the surface of the powder bed with a water/triethylene glycol (TEG) mixture before printing. Results from this study help to build understanding of the physical mechanisms in the BJ printing process that may contribute to formation of defects observed in final parts.

1 Introduction

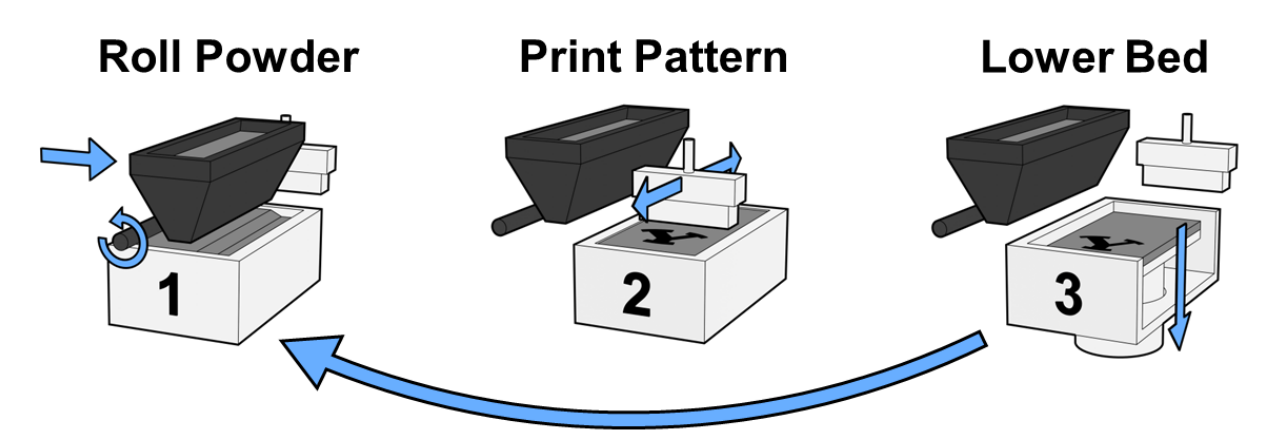


Figure 1: An illustration of three main steps of the printing process in binder jet additive manufacturing. (1) Powder is deposited by a hopper and rolled flat. (2) An inkjet printhead selectively deposits binder onto the powder bed in a desired pattern. (3) the powder bed is lowered, and the process is repeated until the entire part is printed.

Binder jetting (BJ) is an additive manufacturing process where three-dimensional parts are fabricated from a digital CAD model by inkjet printing binder into thin layers of a powder feedstock [1-3]depicted in Figure 1. The resulting green part can be extracted from the powder bed and is typically sintered to obtain desired final part properties. BJ advantages compared to other additive manufacturing processes include relatively high build rates, a wide range of printable powder feedstocks, and comparatively low cost [4, 5]. The inkjet printing process in BJ scales readily for faster, economical production. BJ commonly uses SS316L metal powder feedstocks [6], but the technology can be applied to any powdered material and has been used print in materials such as copper [7], tungsten alloy [8], ceramics [5], and polymers [9].

A significant portion of current research related to BJ focuses on understanding the process to increase final part quality and repeatability for industrial use [7, 10-15]. A key concern in BJ is the residual porosity in printed parts after sintering that negatively impacts part strength and ductility, limiting the use of BJ in demanding industries. Before sintering, green parts typically have densities of 50-60% and require sintering to reach final density [2]. BJ parts printed in stainless steel can reach densities over 99% dense [12]. However, BJ parts experience significant volumetric shrinkage during densification, and if density variation is present in the green part geometric distortion can occur during sintering [16]. Recent work in developing predictive models of part distortion and shrinkage facilitate pre-compensation to improve final part accuracy [17-20]. However, these models cannot account for defects created by printing.

Recent studies suggest that porosity defects are more abundant in regions of the powder bed where binder has been deposited [21-23]. However, the exact mechanisms for increased porosity defects in printed regions is unclear. Salim et al. [21] hypothesize that density variation in bound regions could be caused by voids from binder occupying space in the part. This binder would decompose during sintering to leave a void. Rahman et al. [22] suggest that density variation between bound and unbounded regions of a printed part could be due to residual binder inhibiting the sintering process. Li et al. [23] propose that density variation occurs from differences in packing behavior when rolling over bound and unbound regions from the previous printed layer. Sachs et al. [24] observed disruption of the powder bed from ballistic impact of the binder droplet, and Stevens et al. [25] suggested that powder relocation from ballistic impact and droplet-powder interaction driven by capillary forces could be responsible for the observed density variation.

There is extensive research dedicated to examining the wide field of droplet-powder interaction phenomena [26-33]. Several studies have helped build understanding of droplet-powder interaction in the context of BJ [34-36]. Capillary pressure has been observed to be a major driving mechanism in droplet-powder interaction. Droplet impact regimes have been proposed but have not been tested under inkiet printing conditions typical in BJ as much of the existing research studies the impact of droplets that are orders of magnitude larger and at a fraction of BJ impact speeds [37]. The complex droplet-powder interaction behavior caused by high-speed ballistic impact of micro droplets and subsequent capillary flow into a porous media in the BJ printing process is difficult to observe directly as much of it occurs beneath the surface over very short times scales [2]. Efforts have been made to simulate the BJ printing process to build understanding of droplet impact and imbibition into the powder bed [37-41]. However, BJ process simulation requires models that incorporate complex fluid and multi-body particle dynamics. Tan [37] simulated a micro droplet impacting a powder bed and found that impact velocity affected the binder penetration behavior, but the powder bed was modeled as a static regular grid of rigid spheres and only one spherical droplet was deposited into the powder bed. A static powder bed may be an appropriate simplification for studying binder infiltration behavior but does not capture powder relocation due to droplet impact, which limits insights into mechanisms of defect formation in printed parts.

Several works have directly observed the BJ printing process to better understand droplet-powder interaction behavior. Fan [34] captured high-speed footage of binder droplets impacting alumina powder beds. It was observed that during droplet impact, there is not a clear separation between ballistic impact and penetration into the powder bed. However, the test setup used a continuous inkjet printhead that deposited larger and faster droplets than is typical for modern BJ machines which most commonly use drop-on-demand printheads. Fan reported depositing droplets with a diameter of 87.6 µm (352 picoliter droplet volume) and impact speed of 11.71 m/s, where modern BJ machines typically have droplet volumes of 10-30 pl and droplet velocities ~8 m/s. Additionally Fan reported a printhead excitation frequency of 62.5 kHz, which is significantly higher than the 1-4 kHz typical for drop-on-demand printheads.

In an effort to study the significance of droplet size on droplet-powder interaction, Tan [42] captured high-speed footage of droplets of different sizes impacting nylon powder beds and compared their relative infiltration rates. It was observed that absorption behavior for micrometer-sized droplets was different than millimeter-sized droplets. Droplets significantly larger than powder pore size were found to match models for 3D radial flow, where droplets on the same size scale as the powder pore size were found to follow Washburn 1D flow. Colton et. al. [43] observed that droplet-powder interaction behavior is also affected by temporal and spatial separation of droplets deposited during printing. The observed trends of droplet spacing and droplet inter-arrival time combinations that resulted in successful track formation during printing suggest infiltration behavior consistent with Washburn 1D flow.

Parab et al. [44] used high-speed synchrotron X-ray imaging to directly observe single droplet impacts in conditions more relevant to BJ. The authors used an ExOne X1-Lab printer to print a track of sequentially deposited binder droplets. They observed binder droplet impact on the powder surface and significant powder relocation above and below the powder bed surface. Powder relocation below the powder bed surface was observed to depend on powder material and shape, but other print process parameters relevant to BJ were not studied.

Recent work has shown that previously printed geometry affects droplet-powder interaction behavior [45]. The authors observed that only printing a single line of droplets resulted in different powder agglomeration and track formation behavior than printing geometries comprised of multiple lines of droplets. These findings indicate that observing a single droplet impact, or even a single line of droplets does not fully capture the droplet-powder interaction phenomena in typical BJ printing conditions. Depositing moisture on the surface of the powder bed before printing has also been shown to reduce powder relocation during printing [24, 46]. Inkley et al. [46] found that pre-wetted powder enabled printing at larger droplet spacings, measured reduced surface roughness of printed parts, and qualitatively observed that printing on pre-wetted powder resulted in less powder relocation due to droplet impact.

This work presents observations of droplet-powder interaction from direct high-speed synchrotron X-ray imaging of the BJ printing process. Multiple print process parameters including powder material, print geometry, droplet spacing, powder bed density, and powder bed moisture content were varied to study their effect on droplet-powder interaction phenomena. The effect of the varied print process parameters was studied by measuring powder ejection above the powder bed surface and disturbance of the powder bed beneath the powder bed surface due to droplet impact. Results from this study help build understanding of droplet-powder interaction phenomena in the BJ printing process with the aim of better understanding modes of forming porosity defects in printed BJ parts. The results of this study are also useful to related technologies such as multi jet fusion and high-speed sintering that use inkjet printing on powder feedstocks [47, 48]. Deeper understanding of how droplet-powder interaction is affected by process parameters will help enable the selection of ideal process parameters, inform appropriate simulation models, and improve the design of BJ machines.

2 Methods

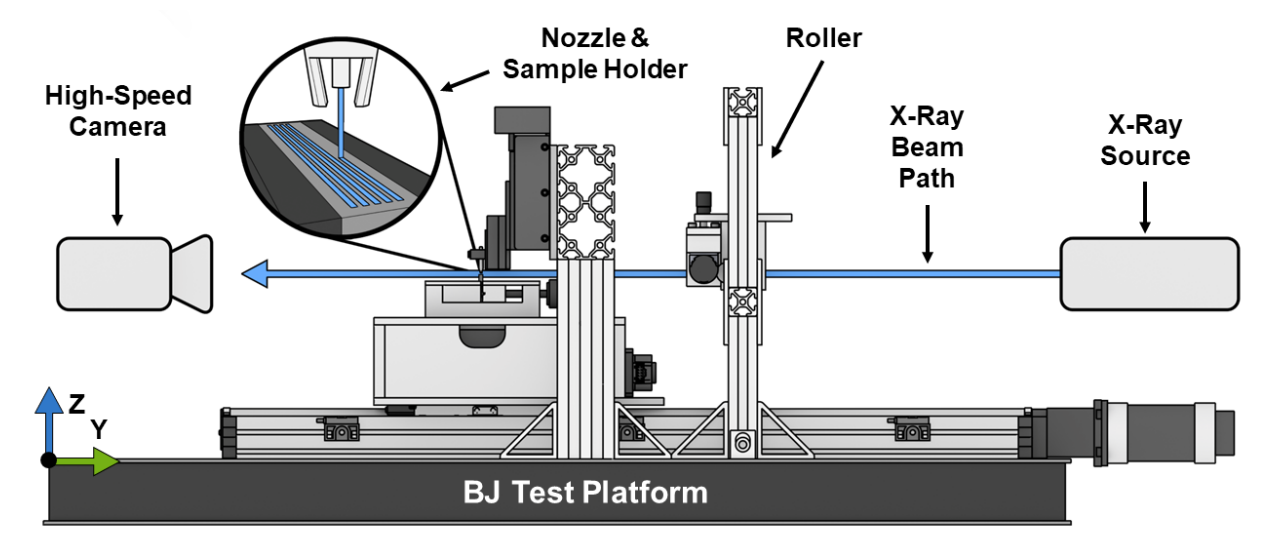


Figure 2: An illustration depicting the experimental setup used for testing. The X-ray beam path travels through the sample and to the high-speed camera. A custom binder jetting system uses a single nozzle printhead to print lines in the sample holder.

2.1 Experimental Setup

Testing was conducted at beamline 32-ID-B at the Advanced Photon Source, Argonne National Laboratory. All testing was performed using a custom binder jetting test platform [49] built for control over process parameters of interest and synchronization with the X-ray beamline. Figure 2 depicts the experimental setup. The test platform has three motion stages for the x, y, and z-axes. The x-axis (Parker mSR100) moves the inkjet printhead and has a bi-directional repeatability of 1.6 µm as reported by the manufacturer. The y-axis moves the z-axis for layer

deposition / printing and has a bi-directional repeatability of 3.0 μ m. The z-axis mounts the sample holder and has a repeatability of 1.0 μ m. The custom printer uses a MicroFab MJ-ABP-01 single nozzle drop-on-demand printhead with a 30 μ m orifice. The printhead was controlled by the MicroFab JetDrive III. Footage of the printing process was captured on a Photron Limited Photron SA-Z. The Photron camera imaged a single crystal Lu₃Al₅O₁₂:Ce scintillator that was used to convert the X-ray beam into visible light. Additional details for the beamline and imaging setup are provided by Parab et al. [44]. Footage was recorded with a pixel scale of 1.98 μ m per pixel and a field of view of 1.27 x 1.19 mm. The camera framerate was set at 50,000 frames per second and the duration of capture for each test was 12 milliseconds.

All tests were conducted using ExOne BA005 aqueous binder. As reported by the manufacturer, the binder density is 1,100 kg/m³, viscosity is 0.0058 Pa*s, and surface tension is 35 mN/m. Droplets were deposited at a jetting frequency of 1024 Hz. Droplet velocity and volume were routinely monitored and controlled during testing. Droplet velocity was measured using a stroboscopic imaging technique and was measured to be 7.5 ± 0.1 m/s. Average droplet volume was obtained by jetting a known number of droplets into a container, which was then massed to obtain an average droplet mass and subsequently droplet volume. Droplet volume was measured to be in the range of 52-63 picoliters during testing. During printing, the droplet formed a single satellite droplet.

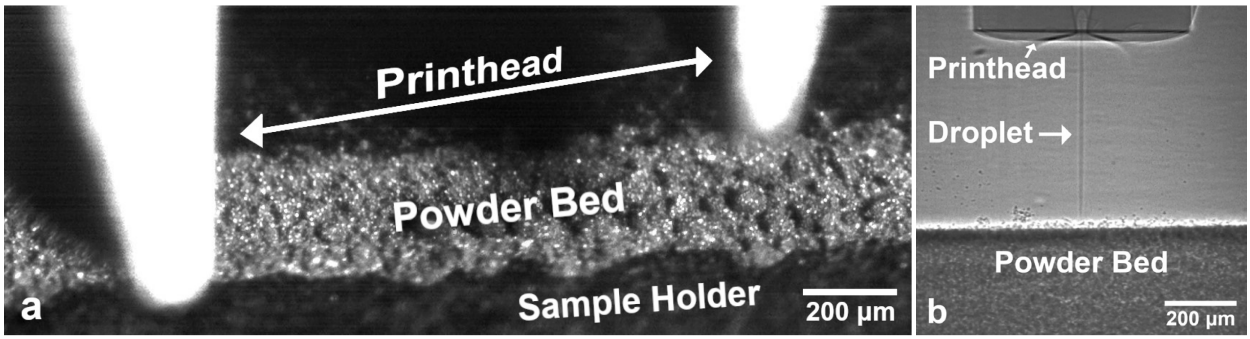


Figure 3: Images of printhead and sample holder during printing. (a) Optical imagery of printing a line in the sample holder. (b) high-speed X-ray imagery of printing.

2.2 Sample Preparation / Testing Process

Loose powder samples were prepared in a glassy carbon sample holder that had a 400 µm wide, 6 mm long, 1.5 mm deep slot with polyimide film tape around the edges of the sample holder to prevent powder from falling out the ends of the slot. Lines were printed along the entire length of the slot, and the camera and X-ray shutter were synchronized to begin capturing images when the nozzle reached the center of the sample holder. Powder was manually deposited into the slot and a blade was used to wipe the powder surface flat. Rolled powder samples were prepared by rolling a 480 µm deep bed of powder with a counterrotating 12 mm roller. The bed was rolled in layers with a 30 µm layer thickness, and the roller traverse speed was 3 mm/s. The rolled powder layer was then trimmed with a razor blade to approximately 500 µm thick in the direction of the X-ray beamline to allow for sufficient X-ray transmission.

2.3 Process Parameters

Five print process parameters were varied during testing including powder material, droplet spacing, printed line number, powder bed density, and powder bed moisture levels. These parameters are defined below. Print direction relative to the beamline was also varied to observe printing both parallel and perpendicular to the image plane.

Table 1: Varied process parameters.

Process Parameter	Tested Range			
Material	SS316L, Glass			
Droplet Spacing	15, 20, 30, 35, 40, 50, 60, 80, 100, 120, 150 μm			
Line Number	1, 2, 3, 4, 5			
Powder Density	Loose, Rolled			
Moisture	Dry, Pre-wetted			

2.3.1 Powder Material

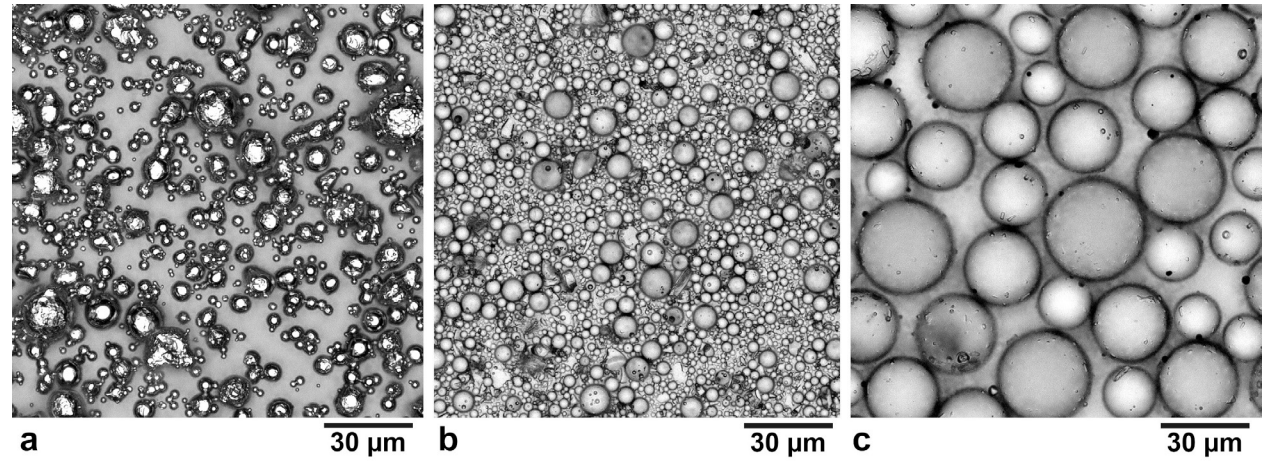


Figure 4: Images of the powder materials used during testing. Images captured on a Keyence VHX-7000. (a) SS316L. (b) 8 μm glass microspheres. (c) 30 μm glass microspheres.

Stainless steel 316L (SS316L) and soda-lime glass microspheres were the powder materials used during testing. Images of the powders are shown in Figure 4. The spherically shaped Sandvik Osprey SS316L powder was produced using gas atomization and has a mean particle diameter (dv50) of 10 μ m, a dv10 of 3.92 μ m and a dv90 of 22.0 μ m [43, 45]. Two sizes of glass microspheres were used. The smaller diameter powder (MO-SCI GL0191B/1-20) was measured to have a mean particle diameter (dv50) of 8 μ m. The larger glass powder (MO-SCI GL0191B4/38-53) was measured to have a mean particle diameter of 30 μ m.

Table 2: Material properties for the tested powder materials.

Material	Mean Particle Diameter (D _{V50})	Material Density	Sample Holder Packing Fraction	Angle of Repose	Contact Angle with Binder
SS316L	10.0 µm	8,00 <mark>==</mark> /m³	46 ± 0.8%	54 ± 1.4°	20 ± 2°
Glass	8.0 µm	2,50 <mark>0′kg</mark> /m³	32 ± 1.1%	54 ± 2.1°	8 ± 2°
Glass	30.0 µm	2,500 kg/m ³	56 ± 0.1%	$34 \pm 1.7^{\circ}$	8 ± 2°

The angle of repose was calculated using the fixed base cone method. A 25.37 mm diameter stainless steel cylinder was used as the base. Powder was deposited onto the base out of a funnel with a 3 mm orifice and slowly lifted as powder was deposited to maintain a fixed height above the top of the powder heap forming on the top of the cylinder. Powder was deposited until the base was entirely covered and the powder heap on the base formed a cone. The height of the cone of powder above the base was measured and was used to calculate the angle of repose using Equation 1 [50]. The angle of repose (θ) is a function of powder height (h) and base diameter

(b). Testing was repeated five times for each powder material and the mean angle of repose is reported.

$$\theta = \tan^{-1} \frac{2h}{h} \tag{1}$$

Contact angle was measured using the captive bubble method on a custom-built optical goniometer. Samples of polished Stainless Steel and soda-lime glass were submerged in binder and an air bubble was trapped on the bottom of the sample using a syringe. The captive bubble was imaged using an IDS UI-3880SE-M-GL USB camera and Edmond Optics 63745 1X telecentric lens. The bubble was backlit by an Advanced Illumination CX0404-WHIIC edge-lit collimated backlight. Contact angle was measured using ImageJ.

2.3.2 Droplet Spacing

The spacing between droplets deposited into the powder bed was varied from 20-150 μ m. The droplet spacings tested were 15, 20, 30, 35, 40, 50, 60, 80, 100, 120, and 150 μ m.

2.3.3 Line Number

Print geometry was varied by printing multiple lines in parallel in the same powder bed and imaging each line being printed. Up to five lines were printed in a single powder bed sample. The spacing between lines matched the droplet spacing, resulting in a regular grid of droplets.

2.3.4 Powder Bed Density

Powder bed density in the SS316L powder was varied by preparing samples either with loose powder or rolled powder. SS316L powder rolled on the custom BJ test platform was measured to have a density of $55 \pm 0.8\%$. Powder bed density was measured by rolling 100 layers (30 µm layer thickness), extracting a section of the powder bed using thin-walled cylindrical plug of a known diameter (38 mm) and weighing the known volume of powder [49]. Loose powder bed density was measured by filling a larger sample holder (20 x 20 x 2 mm) with the powder material, scraping the top surface flat with a blade, and weighing the sample. Three trials were conducted for each material and the results averaged. The loose powder bed density was measured as 46 \pm 0.8%, 32 \pm 1.1%, and 56 \pm 0.1% for SS316L, 8 µm glass, and 30 µm glass respectively.

2.3.5 Powder Bed Moisture

Powder bed moisture levels were varied using an additional moisture application module that was mounted to the printer. Details of the module and application process are described by Inkley et al. [46]. A 4:1 volume mixture of water and tri-ethylene glycol was atomized onto the powder bed surface before printing to study the impact of prewetting on observed droplet-powder interaction phenomena. The sample was left to dry for five minutes after misting to allow for equilibration of moisture content. Inkley et al. [46] found that the mixture partially evaporates but leaves a consistent 34% of the initial deposition after reaching equilibrium.

In total, 201 tests were considered during analysis, with 97 tests conducted in SS316L, 82 in the 8 μ m diameter glass microspheres, and 22 in the larger 30 μ m glass microspheres. Given the difference in X-ray attenuation between SS316L and soda-lime glass, X-ray intensity and camera exposure time were adjusted according to the powder material used. Footage was captured both before and during printing to correct for spatial and temporal variations in intensity in the footage.

2.4 Image Processing

The raw high-speed footage was processed to quantify powder relocation above and below the powder bed surface by tracking powder particles ejected above the powder bed surface and measuring the depth below the powder bed surface that powder was disturbed by droplet impact. The depth below the powder bed surface that powder is disturbed by droplet impact is referred to as "interaction depth" [44]. OpenCV / Python was used for image processing.

2.4.1 Powder Ejection

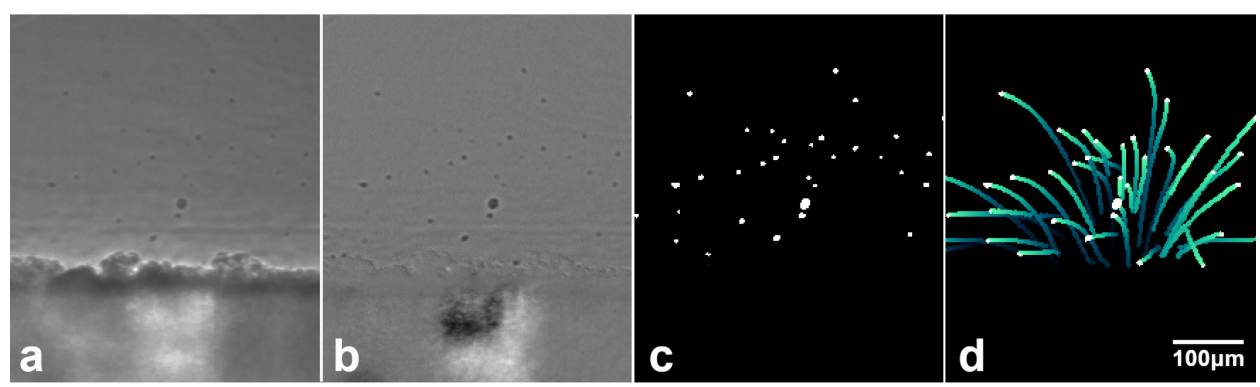


Figure 5: Filtering steps to track ejected powder particles. (a) Footage during printing. (b) Flat-field corrected footage. (c) Adaptive threshold to isolate ejected particles. (d) Tracking results visualized with particle trajectories.

Figure 5 shows steps in processing the raw footage to detect and track ejected powder particles. The print footage is first subtracted from the footage taken before printing to normalize image intensity (flat-field correction). The footage is then cropped to the region above the powder bed and differenced by a temporal gaussian filter to erase slow-moving elements in the footage. An adaptive thresholding filter is applied to obtain a mask that highlights airborne powder particles. The mask is used to detect particles in each frame of the footage. Particles were tracked between frames using the Python TrackPy library. Tracking results were filtered to reduce spurious tracks by metrics such as number of frames tracked, particle start location relative to the bed, and particle displacement. Particle diameter for each tracked particle was estimated from the apparent area of the particle, assuming spherical particles. Only powder particles that were ejected during capture were considered, meaning that powder particles that were already airborne at the start of the footage were discarded from further analysis.

Due to spatial resolution limitations of the captured footage, particles below 4 µm in diameter are not reliably tracked. Additionally, due to the maximum linking distance in the particle tracking algorithm and background subtraction filters used, only particles travelling between 2 and 250 mm/s are tracked. Most newly ejected particles observed were found to be within this speed range.

2.4.2 Interaction Depth

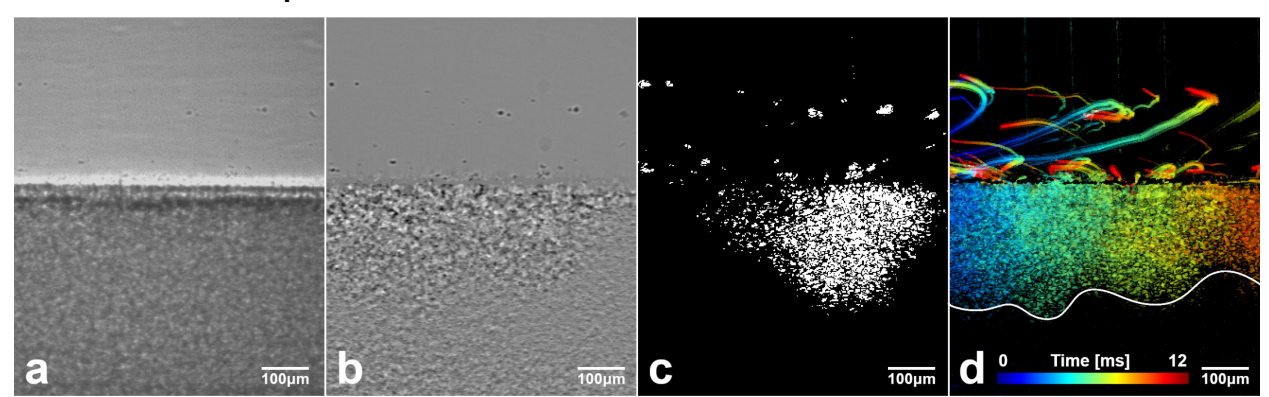


Figure 6: Filtering steps to extract interaction depth from tests. (a) Footage during printing. (b) Flat-field corrected footage. (c) Mask showing image variation due to droplet impact. (d) Color-coded stack showing movement detected in footage and corresponding interaction depth.

Figure 6 shows steps in processing the test footage to obtain an interaction depth. Similar to the processing for ejected particle tracking, the footage is flat field corrected using the footage captured before printing. The value of each pixel in the print footage is divided by the corresponding pixel value before printing and then the logarithm is taken of the result. This normalizes for differences in original X-ray intensity / attenuation. Sudden changes in pixel intensity in the powder bed were detected using OpenCV's mixture of gaussian background subtraction (MoG2) filter. The filter was set to use the previous 10 frames for building the background model and the sensitivity threshold was increased until just before sensor noise began to be erroneously classified as motion. The results from the MoG2 filter were used to mask regions of disturbed powder for each frame. The masks from each frame were summed into a single image and colored according to frame number. Figure 6d shows an example of a merged image. Interaction depth for the test was calculated by tracing the bottom contour of the region where powder disturbance was observed and measuring the mean distance between the contour and the powder bed surface.

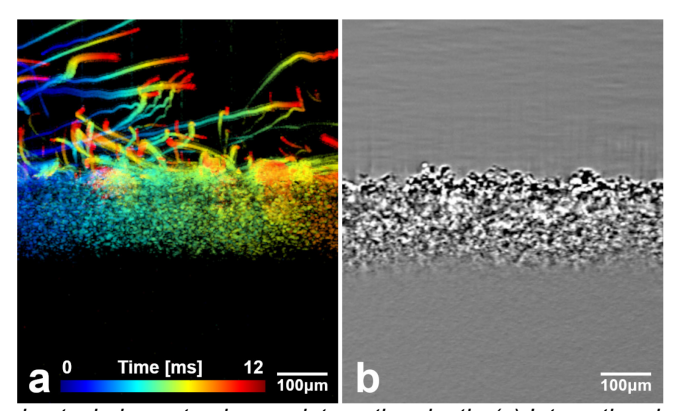


Figure 7: Different processing techniques to observe interaction depth. (a) Interaction depth extracted from motion detected in print footage. (b) Interaction depth extracted from differencing footage captured before and after printing.

The parameters for the processing filters used to calculate interaction depth were optimized to detect the sudden changes in pixel intensity below the powder bed during printing. These sudden changes in pixel intensity corresponding to powder relocation caused by droplet impact dominate the observable variation beneath the powder bed surface during printing. For a few select tests, a still frame of the powder bed after printing was compared to a frame of the bed before printing to highlight differences in the powder caused by the printing process regardless of timescale. Where an interaction depth was extractable using this technique, the depth matched the result

given by the filter applied directly on the print footage. This indicates that the processing filter used on the print footage is successful at detecting the extent of powder relocation in the powder bed, and larger timescale phenomena such as binder infiltration do not visibly disturb the powder bed deeper than the measured interaction depth.

2.5 Part Depth

Supplementary to the high-speed synchrotron X-ray imaging, additional lines were printed on the custom BJ printer and extracted to compare the interaction depth observed in the X-ray imaging with the depth of printed lines. The depth of printed lines corresponds to the depth that powder is bound together by infiltration of binder from the printing process. Comparison of interaction depth and part depth provides insight into how interaction depth relates to the final distribution of binder during the printing process.

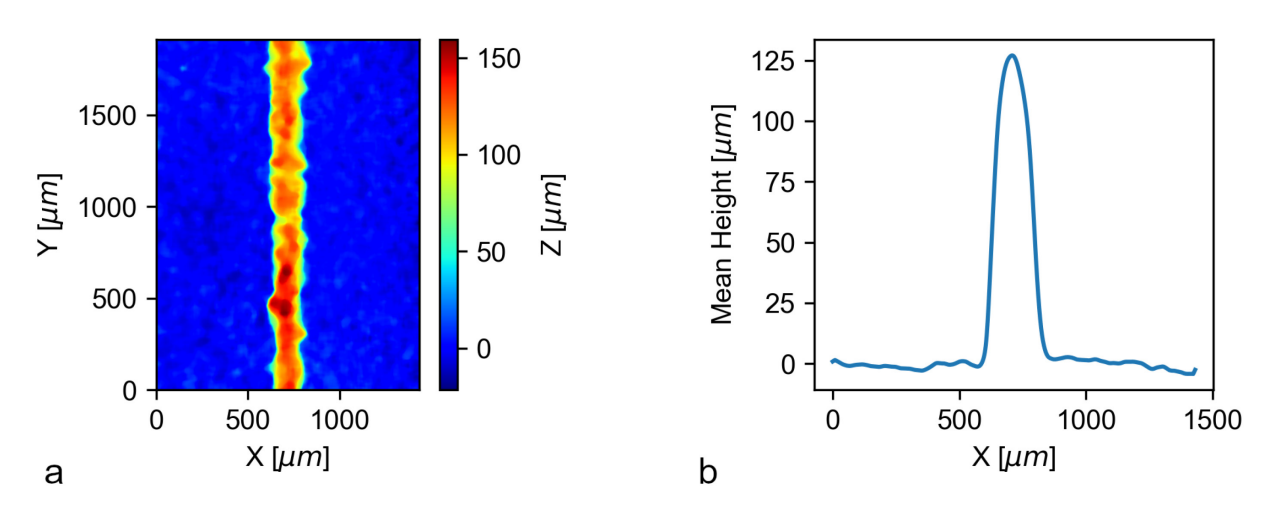


Figure 8: Example of profilometry data of extracted lines printed on the custom BJ system. (a) Profilometry data collected on the Zeta 20. (b) Mean height along the y-axis plotted vs. the x-axis. The part depth is calculated from the maximum value of the curve.

Lines were printed on the custom BJ system in a sample holder measuring 20.4 mm x 20.4 mm x 2.0 mm. Powder samples were prepared by filling the container with the appropriate powder material and then scraping flat with a razor blade. Printer process parameters were set to match those used during X-ray imaging. Droplet spacing was varied between 20-50 µm in 10 µm increments. After printing, the sample holder was moved to an oven and allowed to cure at 180°C for at least 30 minutes. After curing, the lines were extracted from the powder bed using an adhesive film. 1.8 mm long segments of the printed lines were imaged using a Zeta Instruments Zeta 20 optical 3-D profilometer. The resulting height-map image was processed to correct for any tilt in the base the line was resting on. Part depth was calculated by averaging the height along the y-axis and taking the maximum value of the resulting curve. A representative example of the profilometry imagery and subsequent processing is shown in Figure 8.

3 Results / Discussion

3.1 Powder Ejection

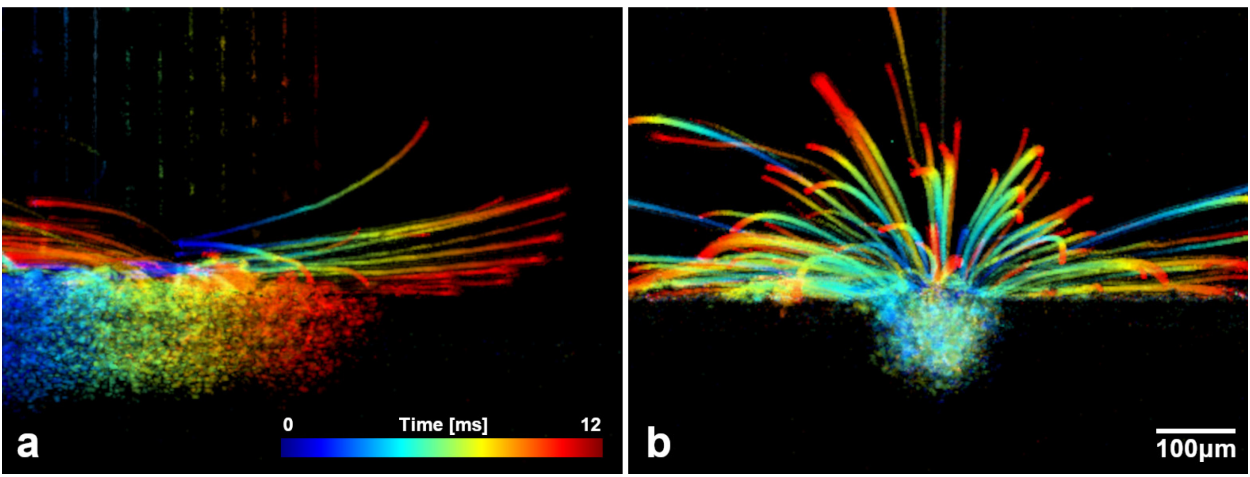


Figure 9: Examples of test footage processed to show powder motion above and below the powder bed surface. Powder ejection is observed above the powder bed surface. (a) Printing direction left to right in 8 μm glass powder. (b) Printing direction normal to image plane in SS316L powder.

In the high-speed X-ray footage, powder particles were observed to eject from the powder bed surface due to binder droplet impact. As described in the methods section, airborne particles were tracked to quantify powder relocation due to ejection and study the effect of varied process parameters.

3.1.1 Powder Material

Figure 10 compares the measured volumetric particle size distribution of the ejected particles observed for each material to the particle size distribution of the powder feedstock. The measured particle size distribution matches the expected distribution well for the larger 30 µm glass powder, but for the SS316L and 8 µm glass powder, particles below 4 µm are not observed to be ejected. This observation matches with the known spatial resolution limitations of the tracking filter.

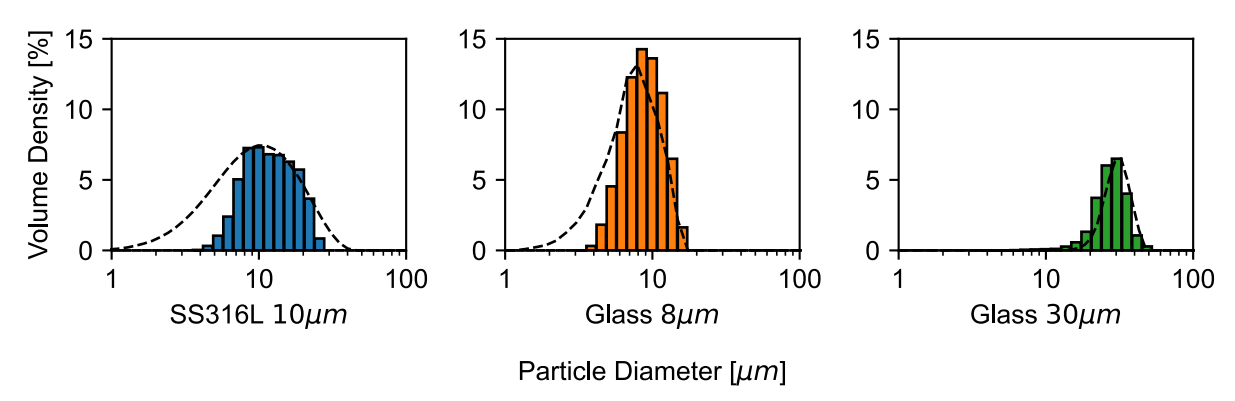


Figure 10: Measured volumetric particle size distribution of ejected particles (shaded box) vs. known particle size distribution (dashed line). Note that due to the resolution of the captured footage, particles below 4 μm in diameter are not tracked reliably.

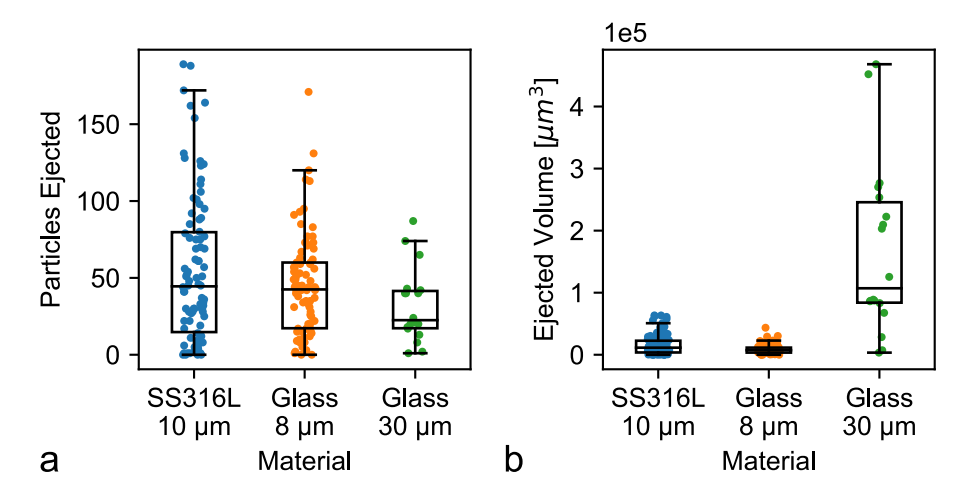


Figure 11: Particle ejection vs. material. (a) Number of particles ejected vs. material. (b) Ejected volume vs. material.

Figure 11 compares particle ejection for the three powder materials tested. Each dot in the graph represents measurement results from an individual test. Figure 11 includes all tests conducted for each material irrespective of droplet spacing, line number, powder bed density, or moisture content. Figure 11a plots the number of particles ejected for each material. For tests that used SS316L powder, a median of 45 particles were observed to be ejected during each test. A median of 43 and 23 particles were observed to be ejected for 8 μm and 30 μm glass respectively. Figure 11b plots ejected volume for each material. Particle volumes were calculated using measured particle diameters and assumed spherical particles. For tests in SS316L powder, a median of 18,000 μm³ was observed to be ejected. For tests in 8 μm glass a median of 7,400 μm³ was observed to be ejected. Tests in 30 μm glass had significantly more volume ejected with a median of 87,000 μm³ of ejected powder and a few tests resulting in over 400,000 μm³ of ejected powder.

The similarity in number of ejected particles between tests that used SS316L and 8 μ m glass powder is worth noting. From observations of ejection behavior in multiple powder sizes and materials, Parab et al. [44] list powder flowability and particle mass as factors that impact powder ejection behavior. The authors suggest that lower density, flowable powders will eject powder more readily during printing. Although the similar measured angle of repose between the SS316L powder and 8 μ m glass powder indicates comparable flowability, the lower measured packing density for 8 μ m glass suggests it has reduced flowability [51, 52]. The reduced flowability of the 8 μ m glass compared to the SS316L powder could explain the similar number of particles ejected despite the lower material density of the glass powder.

The significantly higher ejected volume for 30 μ m glass powder shown in Figure 11b could also be explained by particle flowability. Both the lower angle of repose (34 \pm 1.7°) and higher packing fraction (56 \pm 0.1%) of the 30 μ m glass indicate increased flowability compared to the SS316L and 8 μ m glass powders. This further supports that increased powder flowability could be responsible for increased powder ejection from binder droplet impact.

Tracking ejected particles enables calculation of the ejection velocity of airborne powder particles. Figure 12 shows the calculated ejection velocity by material in both the vertical and horizontal directions of the camera frame. The motion of ejected particles in the direction normal to the imaging plane is not visible. However, SS316L powder lines were measured in orthogonal directions to observe horizontal ejection behavior both parallel and normal to the line printing direction. Imagery processed from footage captured in both orientations is shown in Figure 9. The

mean horizontal ejection speed in SS316L was measured as 89 mm/s and 90 mm/s for the directions parallel and normal to the line printing direction respectively. A t-test yielded a p-value of 0.689, suggesting that there is no significant difference between the ejection speeds parallel and normal to the line printing direction. This suggests that for the current testing conditions, horizontal ejection speed can be assumed to be approximately uniform irrespective of line printing direction.

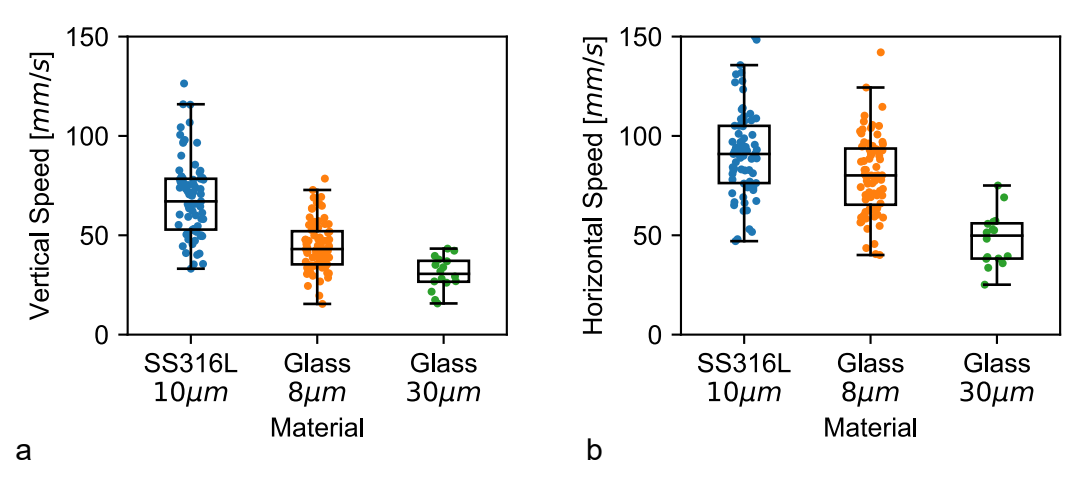


Figure 12: Average ejection velocities of tracked particles by material. (a) Vertical ejection speed. (b) Horizontal ejection speed.

The ejection velocity is calculated from the maximum change in particle position between frames near the start of particle tracking. Mean vertical ejection speed was calculated as 72, 45, and 35 mm/s for SS316L, 8 µm glass, and 30 µm glass respectively. Mean horizontal ejection speed was calculated to be 89, 82, and 46 mm/s. The measured 72 mm/s mean vertical speed agrees with the results from Yang et al. who performed particle tracking on the footage captured by Parab et al. and calculated a mean vertical ejection speed of 75.44 mm/s for a test in SS316L powder [53].

It is noteworthy that ejection velocity for the SS316L powder is higher than for the 8 µm glass powder. Given the larger particle size and density of the SS316L powder compared to the 8 µm glass powder, ejecting a SS316L powder particle requires a significantly larger transfer of pentum. This suggests that larger net forces are being applied to the SS316L powder pared to the glass powder to cause powder ejection.

Given that droplet volume and velocity were held constant for all tests and that particle size distributions for the SS316L and 8 µm glass are comparable, differences in forces on the powder most likely come from differences in binder infiltration mechanics rather than ballistic impact. Binder infiltration is largely driven by capillary pressure, which can be calculated using the Young-Dupré equation:

$$P_{cap} = \frac{2\gamma \cos \theta}{r} \tag{2}$$

Capillary pressure (P_{cap}) is a function of surface tension (γ), contact angle (θ), and pore radius (r). Measured contact angle of the powders is listed in Table 2. The surface tension of the binder was reported as 35 mN/m by the manufacturer. Pore radius can be estimated by using the Kozeny approach [54]:

$$r = \frac{d_{32}\epsilon}{3(1-\epsilon)} \tag{3}$$

Pore radius (r) is a function of the Sauter mean diameter of the powder (d_{32}) and the powder bed porosity (ϵ) . While the d_{32} values are similar for the SS316L and 8 μ m glass powders, the higher contact angle and lower measured porosity of the SS316L powder compared to the glass powder will result in lower capillary pressures in the SS316L powder. Capillary pressure in the powder bed serves to increase inter-particle cohesion [55]. The lower magnitude of capillary pressures in the SS316L powder may cause powder to eject more readily and at a higher velocity compared to the glass powders.

3.1.2 Powder Rolling

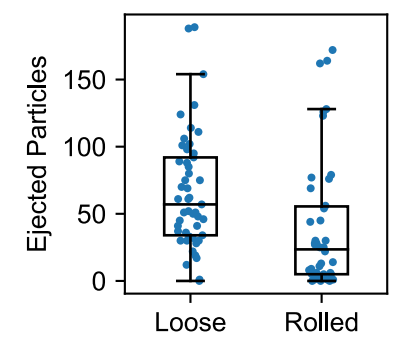
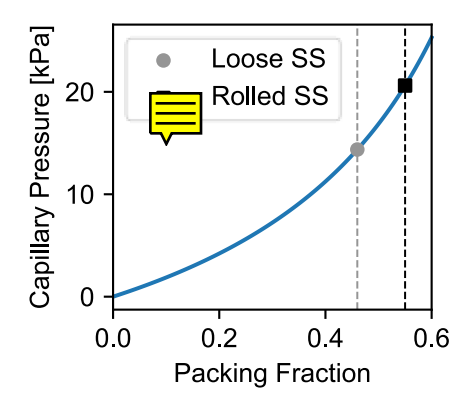


Figure 13: Number of ejected particles for loose and rolled SS316L powder samples.

Powder rolling condition was found to be significant in powder ejection behavior. Figure 13 shows that the average number of particles ejected in rolled SS316L samples is observed to be lower than in loose powder bed samples. This reduced ejection in rolled SS316L powder could be explained by an increased capillary pressure present in the powder bed compared to loose SS316L powder. Figure 14 plots theoretical capillary pressure derived from Equations 2 and 3 in SS316L as a function of powder bed packing fraction. The higher packing fraction of the rolled samples decreases the effective pore radius, thereby increasing the capillary pressure. The resulting increase in inter-particle cohesion in rolled beds may lower the number of particles ejected. Another possible reason for the reduced ejection is a higher degree of mechanical interlocking of the particles due to the increased coordination number when they are compacted by the roller [56]. Increased mechanical interlocking would increase the force required for particles to be ejected from the powder bed, thereby reducing the total number of particles ejected.



Figu : Theoretical capillary pressure in SS316L powder as a function of powder bed density.

Looking at the velocity of ejected particles in loose vs. rolled SS316L, a few interesting trends appear. As shown in Figure 15a, the average vertical speed of particles ejected from rolled SS316L powder was observed to be higher than the speed of particles ejected from loose SS316L powder. In contrast, the horizontal speed (Figure 15b) of particles ejected from rolled SS316L is slightly lower than the speed of particles ejected from loose SS316L powder. Figure 15c shows an estimate of the total kinetic energy of ejected particles for loose and rolled SS316L. For each detected particle, particle mass was estimated from the apparent particle diameter, and particle speed was estimated from both the vertical and horizontal speed components, noting that motion in and out of the imaging plane cannot be observed. The total kinetic energy of ejected particles is observed to be similar between loose and rolled SS316L. Although the mechanisms responsible for these observations are unclear, the observed difference in vertical ejection speed provides additional evidence that powder relocation behavior is dependent on powder rolling condition. Additionally, the reported ejection velocity and kinetic energy may be used to validate simulation models of the BJ printing process.

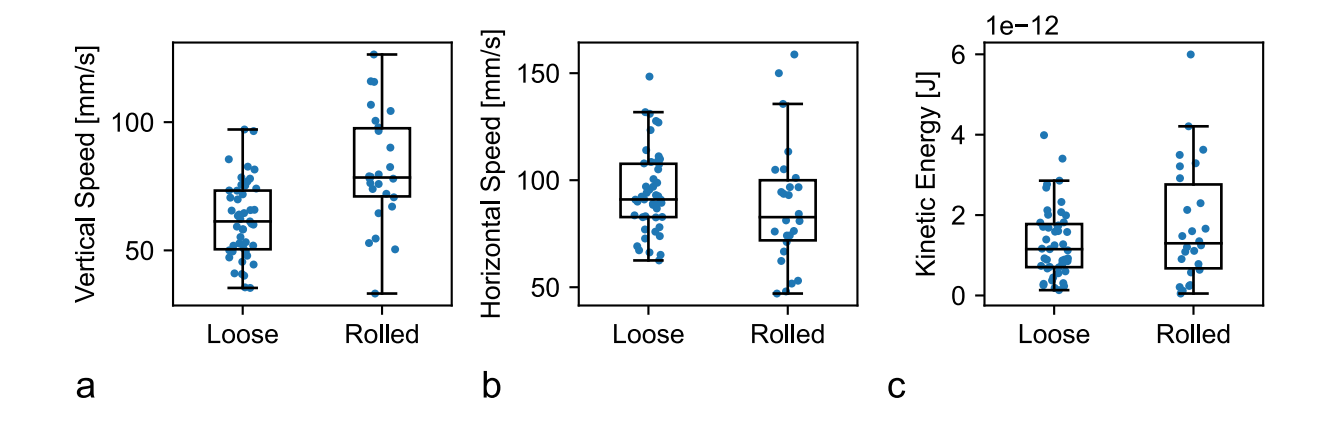
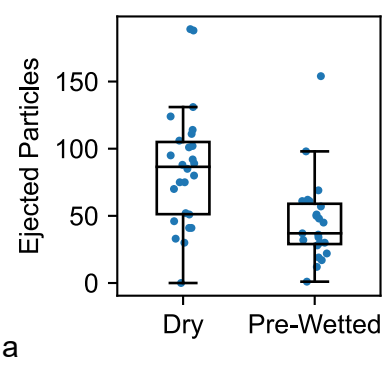


Figure 15: Ejection speed and estimated kinetic energy compared between loose and rolled SS316L samples. (a) vertical ejection speed for loose and rolled SS316L samples. (b) Horizontal ejection speed. (c) Kinetic energy for loose and rolled SS316L samples. Particle mass is estimated from the observed particle diameter and assumes a spherical particle. Particle speed is estimated from the vertical and horizontal components.

3.1.3 Pre-Wetting



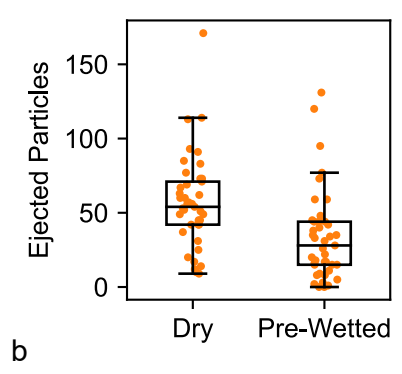


Figure 16: Number of ejected particles for dry vs. moisture treated powder. (a) Results for SS316L powder. (b) Results for 8 µm glass powder.

Another process parameter affecting powder ejection was the application of moisture on the powder bed before printing. As seen in Figure 16, samples that were treated with water/triethylene glycol (TEG) mixture before printing showed on average 46% less ejection in SS316L and 41% less ejection in 8 µm glass than untreated, or dry, powder. These results support the findings of Inkley et al. [46] regarding the reduction of powder relocation in pre-wetted powders and the reported qualitative observations on relative ejection between dry and pre-wetted powder. Increased powder cohesion and droplet infiltration rate in moisture treated powders were suggested as possible reasons for the observed decrease in powder relocation.

3.1.4 Droplet Spacing

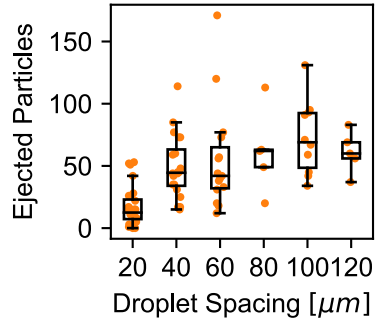


Figure 17: Number of ejected 8 µm glass particles vs. droplet spacing.

The number of ejected particles was also found to be sensitive to droplet spacing. Figure 17 plots the number of ejected particles with respect to droplet spacing in 8 µm glass powder. A general trend of increasing ejection as droplet spacing increases can be observed. Yang et al. [53] found the same trend in their simulation work. They reasoned that at large droplet spacings more powder is affected by binder impact and less of the kinetic energy of binder droplets is damped. Tests conducted with higher droplet spacings resulted in a longer printed line during X-Ray exposure, and hence more powder particles affected by binder impact, but each test had the same number of droplet impacts during exposure. This suggests that ejection behavior is different when depositing a droplet near a previously deposited droplet.

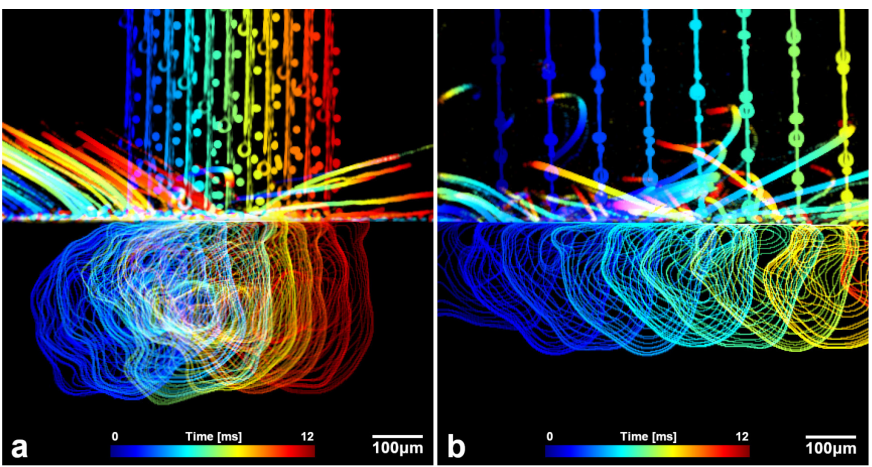


Figure 18: Processed footage showing droplet trails and regions beneath the powder affected by impact in 8µm glass powder for different droplet spacings. (a) 40 µm droplet spacing. (b) 100 µm droplet spacing.

Figure 18 illustrates the observed effect of droplet spacing and shows two tests printed in 8 μ m glass powder at droplet spacings of 40 μ m (Figure 18a) and 100 μ m (Figure 18b). The processing filter outlined the regions of the powder bed disturbed by droplet impact. As droplet spacing increases, the overlap of these regions decreases. Although the exact correlation between disturbed powder and presence of binder is unclear, at lower droplet spacings more of the region where a new droplet impact is already moistened by prior droplets. The mechanism responsible for differences in powder ejection with respect to droplet spacing could be similar to the mechanism responsible for the difference in ejection behavior seen in powder beds treated with the water/TEG mixture. Both tests show decreased ejection with increasing moisture content in the powder bed at the droplet impact site. Addition of moisture into powders has been shown to increase inter-particle cohesive forces [57]. Increased cohesive forces could explain the reduced ejection seen when increasing powder bed moisture content via water/TEG mixture treatment and lower droplet spacings. Increased permeability of wetted powder could also explain the observed differences.

3.1.5 Line Number

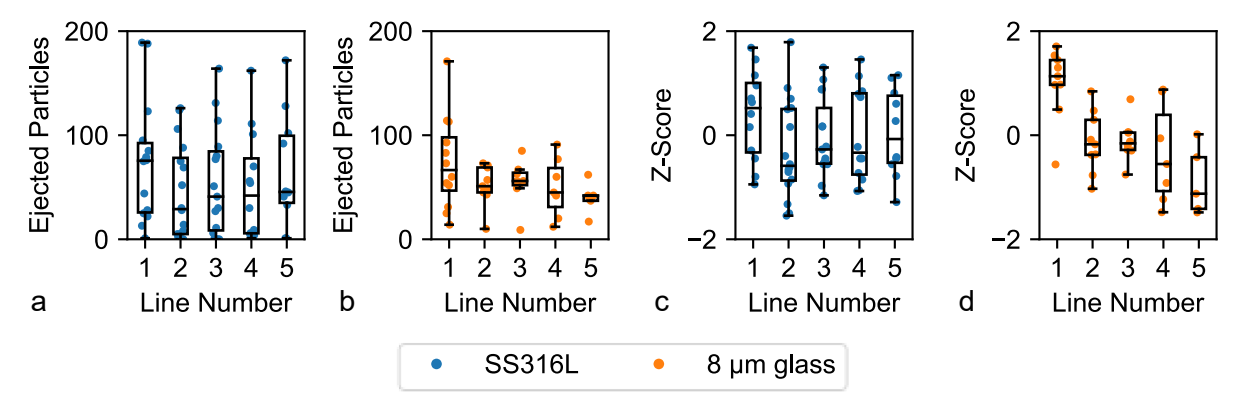


Figure 19: Number of ejected particles and relative ejection vs. line number in dry samples. (a) Number of ejected particles vs. line number in dry SS316L. (b) Number of ejected particles vs. line number in dry 8 μm glass. (c) Relative ejection vs. line number in dry SS316L. (d) Relative ejection vs. line number in dry 8 μm glass.

The last varied process parameter affecting ejection behavior was the printed line number. Figure 19 plots the number of ejected particles vs. line number for each set of printed lines. In each sample, up to 5 lines were printed in sequence and printing of each line was imaged. The

separation between each line matched the droplet spacing. For each test, the z-score (i.e. number of standard deviations from the mean) of the number of ejected particles was calculated relative to the other lines printed in the same sample. The average number of ejected particles for the first line is observed to be higher than for subsequent lines in all materials. The trend is strongest in in the $8 \mu m$ glass powder (Figure 19d).

Again, this observation could be explained in the context of presence of moisture / binder in the bed. When printing the first line, there is no binder in the powder bed and the powder behaves as dry powder. But on subsequent lines, binder is being deposited on powder that has at least been partially wetted by binder from previous lines and behaves more like wetted powder. This conclusion is supported by the fact that this trend is only seen in the dry powder. The first printed line does not have higher ejection relative to subsequent lines in pre-wetted powder.

This result supports the observations made by Colton et al. that droplet-powder interaction behavior is affected by previously printed geometry [45]. Powder relocation was reduced for droplets deposited close to previous droplets. Given that each layer in the BJ process is comprised of many closely spaced droplets, droplet and line spacing could have a significant impact on the quantity of powder relocation. The printhead used for this testing only has one nozzle and each line was printed in sequence, but for multi-nozzle printheads commonly used in commercial BJ machines, careful consideration of rasterizing strategies may yield relatively lower powder ejection due to droplet impact.

3.1.6 Volume of Ejected Powder

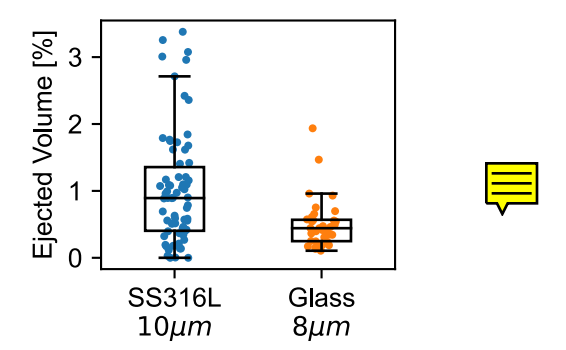


Figure 20: Percent ejected volume vs. material.

Results from the particle tracking analysis can be used to estimate the total ejected volume. The observed ejected volume is divided by the number of droplets in the video to get an average volume of powder ejected per droplet. This volume is then divided by an estimate of the expected volume of bound powder per droplet to yield a percentage ejected volume. The estimate of expected volume of bound powder is calculated from the droplet volume, an estimated saturation ratio of 70%, and a powder bed density of 50%. This volume percentage provides a rough estimate of the proportion of powder that is ejected to understand the significance of powder ejection. As shown in Figure 20a mean of 1% of the powder was observed to be ejected in SS316L prints with a max of over 3%. In tests that used 8 µm glass powder, a mean of 0.5% of the powder was observed to be ejected. For comparison, Salim et al. observed that printed zones experienced a 16% reduction in density in stainless steel powder [21]. Others have similarly seen a reduction of powder density in regions where droplets impact the powder bed during printing [22, 23]. Powder ejection measured here would not account for the full decrease observed. However, even a 1% decrease in powder density due to printing will contribute to reduced part accuracy or increase final porosity. The observed density changes in printed zones may be a

result of multiple modes of powder relocation including ejection, powder relocation below the powder bed surface, and inter-layer effects.

3.2 Interaction Depth

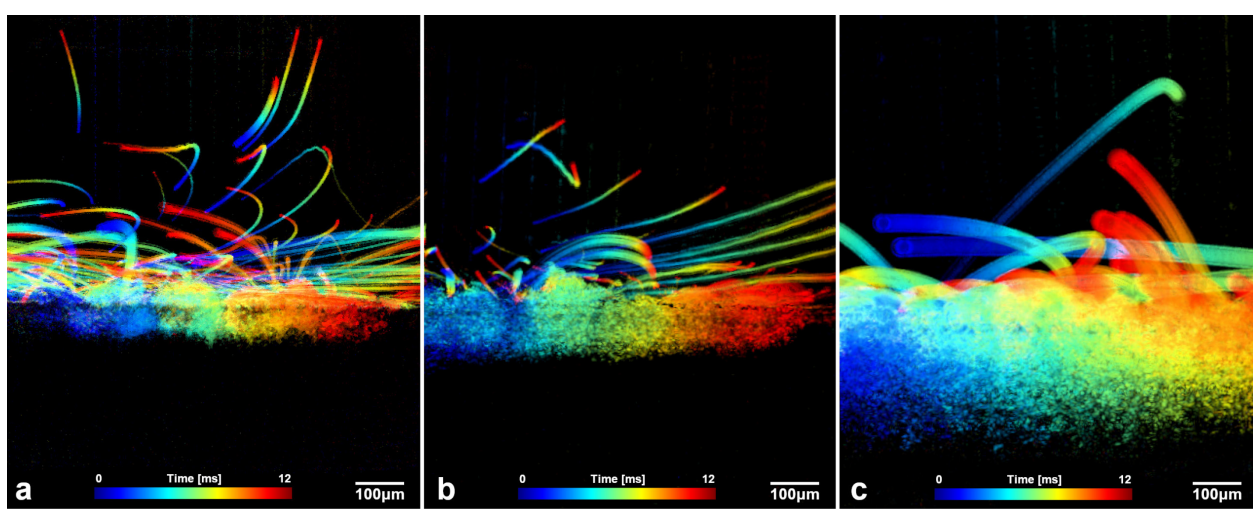
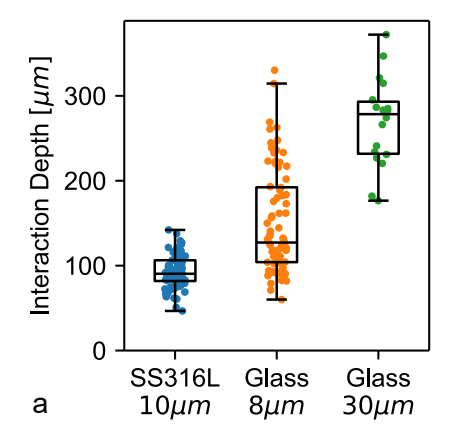


Figure 21: Examples of imagery processed to measure interaction depth for each tested material. (a) SS316L. (b) 8 μm glass. (c) 30 μm glass.

The other mode of powder relocation covered in this work is powder relocation beneath the powder bed surface due to droplet impact. In the X-ray footage, the powder bed beneath the location of droplet impact is disturbed in the ~0.1-0.3 ms following droplet impact. Parab et al. also observed this mode of powder relocation and referred to it as interaction depth [44]. Interaction depth is defined as the depth below the powder bed surface that powder is observed to be disturbed by droplet impact. Powder bed disturbances are detected by local changes in pixel intensity in the X-ray footage, corresponding to a change in the quantity of attenuating material in the path of the X-ray.

3.2.1 Powder Material



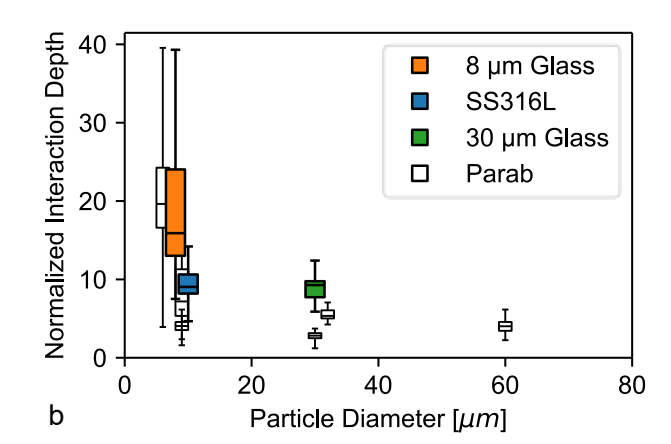


Figure 22: Interaction depth for each tested powder material. (a) Interaction depth. (b) Normalized interaction depth by mean particle diameter (d_{V50}) combined with data collected by Parab et al. [44].

Figure 22 shows interaction depths for each powder material used in testing. Interaction depth is observed to vary more strongly with powder material than the particle ejection. The mean interaction depths were measured as 93, 151, and $269 \mu m$ for SS316L, $8 \mu m$ glass, and $30 \mu m$

glass respectively. Comparing the materials used in testing, interaction depth appears to increase for larger powders. The figure on the right plots the measured interaction depth normalized by mean particle diameter (d₅₀). While Parab et al. reported a lower normalized interaction depth for a similar SS316 powder [44], the trend in normalized interaction depth vs. particle diameter is similar to the present work. The discrepancy in measured interaction depth likely comes from differences in experimental setup. The custom BJ system used for this testing dispensed larger droplets (55 pl) than X1-Lab printer used in the other study (30 pl), which could account for the increased interaction depths observed in this study.

3.2.2 Interaction Depth vs. Infiltration Depth

It is important to note that the observed interaction depth presented here is a result of observable movement of X-ray attenuating material underneath the powder bed. Movement of powder and movement of binder are not easily differentiated in the X-ray footage, meaning that interaction depth is not necessarily the same as binder infiltration depth. Binder infiltration is largely driven by capillary forces in the powder bed and likely occurs over a much larger time scale than the phenomenon observed here. To study the timescale of powder relocation below the powder bed surface due to droplet impact, the processed footage used to obtain interaction depth was used to extract a characteristic time between droplet impact and the end of particle motion from the impact. Figure 23 shows a plot of the area of each frame that was classified as disturbed powder by the processing filters (mask area) as described in the methods section. Clear spikes are seen corresponding to powder disturbance immediately following droplet impact. The beginning of each spike corresponds closely with the droplet impact in the footage. The number of frames between droplet impact and following maximum disturbed area can be used to estimate the timescale over which the interaction phenomenon takes place.

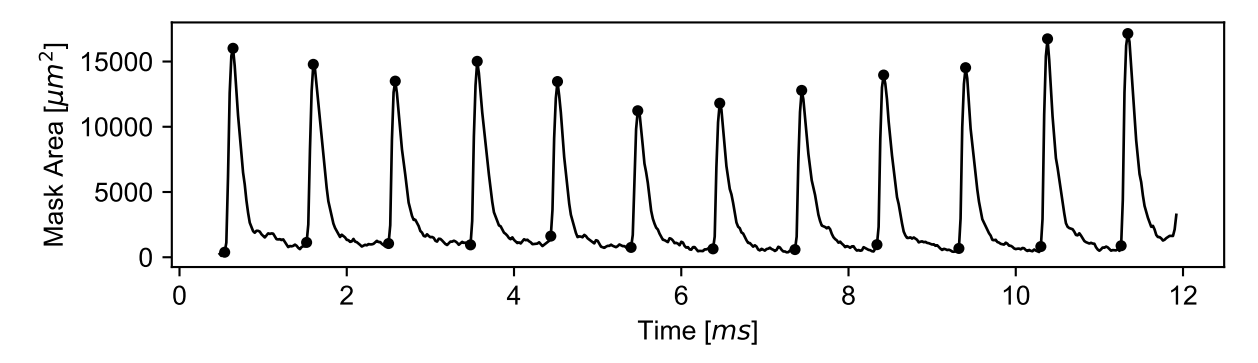


Figure 23: Mask area for each frame after processing footage to detect disturbance beneath the powder bed due to droplet impact.

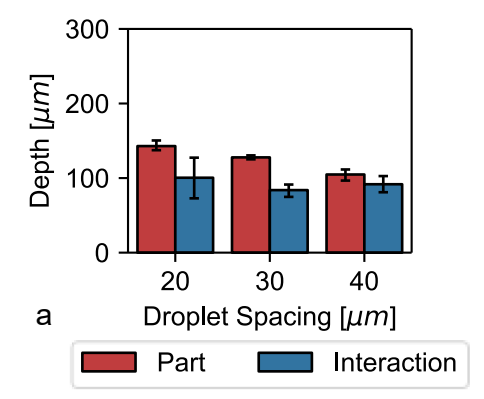
Although an interaction depth could be extracted for all of the powder materials tested, due to the increased X-ray attenuation of SS316L compared to glass, the characteristic timescale is only reliably extractable for the glass powders. The mean time between droplet impact and the end of powder disturbance in the glass powders was 0.1 ms. Dividing the measured interaction depth by the mean powder disturbance time, a mean powder disturbance propagation speed can be estimated. In the 8 μ m glass powder, this speed was calculated as 1.9 m/s. It should be noted that only the rising edge of the spike was used for analysis as the shape of the falling edge of the spike is affected by the filter parameters used to detect powder disturbance.

To compare the observed phenomena to an expected timescale of binder infiltration, the Washburn infiltration model can be used to model binder flow through the powder bed. Tan found

that the Washburn model matched experimental imbibition behavior of inkjet micro droplets into powder beds [42]. The Washburn equation is given as [58]:

$$h = \sqrt{\frac{\gamma r \cos \theta}{2\eta}} t \tag{4}$$

The depth of infiltration (h) is a function of binder surface tension (γ), effective pore radius (r), contact angle (θ) , binder viscosity (η) , and time (t). The binder surface tension and viscosity are 35 mN/m and 0.0058 Pa*s respectively as reported by the manufacturer. Measured contact angle for each material is reported in Table 2. Effective pore radius can be obtained from Equation 4. Assuming the average penetration depth of 180 µm as measured for the 8 µm glass, the Washburn model predicts a penetration time of ~5 ms. This is a significantly longer timescale than that from the observed powder bed disturbance. Fan [34] captured high-speed footage of microdroplet impacts on a powder bed and observed that there was not a clear separation between the stages of droplet impact and fluid penetration, suggesting that the phenomena need to be considered together for BJ printing conditions. The kinetic energy of impact may increase infiltration rates compared to the Washburn model, but from the footage alone it is difficult to distinguish binder infiltration from powder relocation. However, the geometry of printed lines provides a helpful comparison. Figure 24 compares the interaction depth obtained from X-ray footage for SS316L samples and the measured part depth of extracted lines printed under similar printing conditions. Part depth is observed to decrease linearly with droplet spacing. This result is intuitive considering the smaller quantity of binder deposited at higher droplet spacings. Interaction depth vs. droplet spacing does not show the same trend. Additionally, the SS316L parts have larger part dimensions than the interaction depth for smaller droplet spacings. These discrepancies indicates that infiltration depth does not directly correlate with binder infiltration depth.



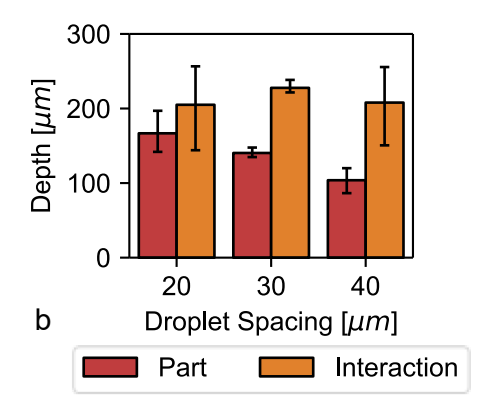


Figure 24: Measured part depth vs interaction depth. (a) Part vs. interaction depth for SS316L samples. (b) Part vs. interaction depth for 8 µm glass samples. Part depth shows a decreasing trend with droplet spacing not present in interaction depth.

3.2.3 Pre-Wetting

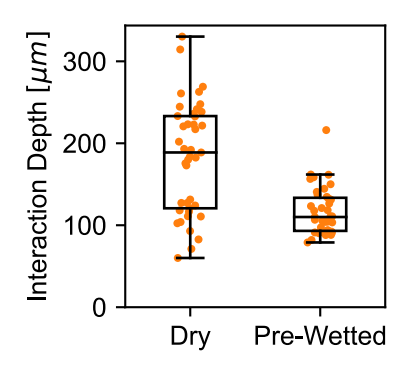


Figure 25: Interaction depths of dry and pre-wetted 8 µm glass.

As shown in Figure 25, interaction depth is observed to be reduced by adding moisture to the powder bed before printing in 8 µm glass powder. This follows the same trend as was seen for powder relocation via ejection. However, this trend was only seen in the 8 µm glass, and interaction depth was not found to be sensitive to moisture levels for SS316L powder. Other parameters, such as rolled vs. loose, droplet spacing, and line number were not observed to have a significant impact on interaction depth in either the SS316L or 8 µm glass powders. Given that sensitivity to those parameters were seen in the ejection results described earlier, the lack of clear trends indicates that the driving mechanism for interaction depth is different than that for ejection. While the process parameters that affected ejection seemed to be related to binder-powder infiltration behavior, interaction depth behavior may be driven by a different mechanism such as the kinetic energy of droplet impact.

Parab et al. [44] reported that the interaction depth for large spherical powders followed a model for crater size proposed by Katsuragi [59]. They also noted that interaction depth for small diameter powders was significantly higher than predicted and speculated that the reason was an increase in momentum transfer via higher cohesive forces present in smaller powders. However, addition of moisture into a powder bed has been shown to increase cohesive forces [57] but reduced interaction depth in this study. This indicates a more complicated relationship between powder bed cohesion and interaction depth. The effect of application of the water/TEG mixture used in this study on powder bed cohesion, interfacial tension, and permeability needs to be studied further to better understand the mechanism responsible for the observed reduction in interaction depth.

Powder relocation beneath the surface of the powder bed is also indicated by the width of powder disturbed by individual droplet impacts. This is referred to as impact width in this study and was only extractable in the 8 µm glass powder where the profile of disturbed powder could be measured for each frame. The frame that contained the largest profile of disturbed powder after each droplet impact was considered and a bounding box around the profile was used to measure the impact width.

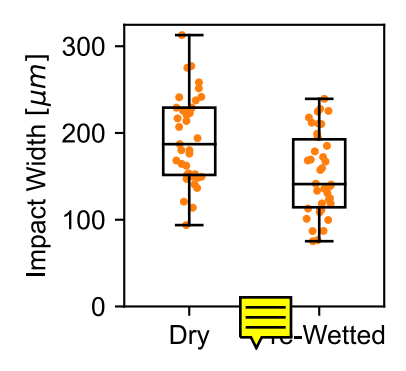


Figure 26: Impact widths of dry and pre-wetted 8 μm glass.

As seen in Figure 26, impact width is reduced by pre-wetting the powder bed in the 8 µm glass. Given both the reduction in interaction depth and impact width, pre-wetting the powder bed reduces the total amount of powder disturbed by each droplet impact. This observation is notable in context of the observations made by Inkley et. al [46] regarding infiltration behavior in powders treated with a TEG/water mixture. The authors reported that the line width of printed parts increased with applied moisture content, indicating that application of the water/TEG mixture encouraged horizontal spreading of binder in the powder bed. Conversely, impact width is shown to be reduced in powder beds treated with the water/TEG mixture, further indicating that interaction phenomenon observed in this study is fundamentally different than binder infiltration behavior, and that moisture in the powder bed affects how powder reacts to the ballistic impact of binder droplets.

3.2.4 Droplet Spacing

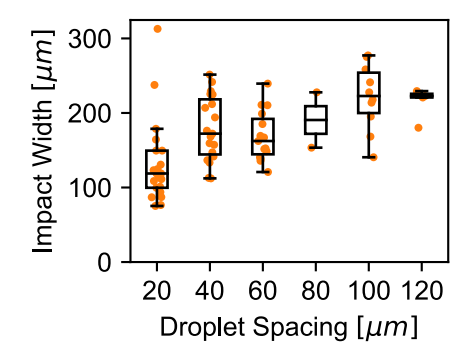


Figure 27: Impact width vs. droplet spacing for 8 µm glass.

Impact width is also observed to increase with droplet spacing in 8 µm glass powders. This follows the same trend seen for powder relocation by powder ejection. Lower droplet spacings result in higher levels of moisture in the powder bed and given that the lowest droplet spacings have the lowest impact width, this result is another indication that moisture in the powder bed reduces powder bed relocation due to ballistic impact of binder droplets.

4 Conclusion

This study provides new insight into the droplet-powder interaction phenomena during the binder jet additive manufacturing printing process. High-speed synchrotron X-ray imaging of the printing process enabled quantification of powder ejection above the powder bed surface and powder disturbance below the powder bed surface due to droplet impact.

Summary of Key Findings:

Powder Ejection:

- Powder ejection is influenced by multiple parameters, including powder material, spreading condition, pre-wetting, geometry, and droplet spacing.
- Rolled SS316L powder beds experienced a reduced number of ejected powder particles and increased average ejection velocity compared to loose beds.
- Printing near previously deposited binder leads to reduced powder ejection.
- Surfaces treated with a water/TEG mixture exhibit less powder ejection.
- Powder ejection can be reduced by using rolled beds, printing near previously printed powder, and pre-treating with a water/TEG mixture.
- The volume of ejected powder was estimated to be ~1% of the printed volume in SS316L powder, suggesting that multiple modes of powder relocation contribute to density changes in printed zones.

Sub-Surface Powder Relocation:

- Sub-surface powder relocation, quantified using interaction depth and impact width, is most sensitive to the powder material used.
- Interaction depth is found to be not tightly correlated with infiltration depth.
- Contrary to prior work, increased cohesion (due to water/TEG treatment) reduces subsurface powder relocation caused by droplet impact.
- Smaller droplet spacings also reduce sub-surface powder relocation.

The print process parameters that had the greatest effect on powder relocation behavior including the application of a water/TEG mixture, lower droplet spacings, and higher line numbers all increase moisture in the powder bed, indicating that moisture in the powder bed during printing plays a significant role in binder-powder interaction behavior. Consideration of moisture present in and added to powder beds in the design of BJ machines and selection of process parameters could help to reduce powder relocation during the printing process and aid in producing higher quality BJ parts. When considering future experiments or simulation models, care should be taken to consider the effect of other droplets or moisture in the powder bed, and simulation volumes should be sized appropriately to capture the extent of sub-surface powder relocation due to droplet impact.

In future work, rheology of dry and water/TEG moisture treated powders could be compared to study the mechanisms that cause reduced powder relocation in treated powders. Measuring and comparing infiltration rates of dry and pre-wetted powder could further elucidate mechanisms for the observed reduction in powder ejection. Future synchrotron imaging of the BJ printing process could vary droplet volume and velocity to study the effect on powder relocation via interaction depth. Additionally, alternative rasterizing strategies could be studied for multi-nozzle printhead systems to study the effect of printing next to bound vs. unbound powder on final part density.

Acknowledgements

This material is based upon work supported by the National Science Foundation through award number CMMI-1946724 and NRC 31310019M0006.

Disclaimer: Any opinions, findings, and conclusions or recommendations expressed in this material are those of the author(s) and do not necessarily reflect the views of the National Science Foundation.

This research used resources of the Advanced Photon Source, a U.S. Department of Energy (DOE) Office of Science user facility operated for the DOE Office of Science by Argonne National Laboratory under Contract No. DE-AC02-06CH11357.

References

- [1] M. Ziaee, N.B. Crane, Binder jetting: A review of process, materials, and methods, Additive Manufacturing, 28 (2019) 781-801.
- [2] A. Mostafaei, A.M. Elliott, J.E. Barnes, F. Li, W. Tan, C.L. Cramer, P. Nandwana, M. Chmielus, Binder jet 3D printing—Process parameters, materials, properties, modeling, and challenges, Progress in Materials Science, 119 (2021) 100707.
- [3] E. Sachs, M. Cima, J. Cornie, Three-dimensional printing: rapid tooling and prototypes directly from a CAD model, CIRP annals, 39 (1990) 201-204.
- [4] M. Li, W. Du, A. Elwany, Z. Pei, C. Ma, Metal Binder Jetting Additive Manufacturing: A Literature Review, Journal of Manufacturing Science and Engineering, 142 (2020) 1-45.
- [5] E. Sachs, M. Cima, J. Bredt, A. Curodeau, T. Fan, D. Brancazio, CAD-casting: direct fabrication of ceramic shells and cores by three dimensional printing, Manufacturing Review, 5 (1992) 117-126
- [6] S. Mirzababaei, S. Pasebani, A review on binder jet additive manufacturing of 316L stainless steel, Journal of Manufacturing and Materials Processing, 3 (2019) 82.
- [7] Y. Bai, C.B. Williams, An exploration of binder jetting of copper, Rapid Prototyping Journal, 21 (2015) 177-185.
- [8] M.T. Stawovy, K. Myers, S. Ohm, Binder jet printing of tungsten heavy alloy, International Journal of Refractory Metals and Hard Materials, 83 (2019) 104981.
- [9] B.M. Wu, S.W. Borland, R.A. Giordano, L.G. Cima, E.M. Sachs, M.J. Cima, Solid free-form fabrication of drug delivery devices, Journal of Controlled Release, 40 (1996) 77-87.
- [10] H. Chen, Y.F. Zhao, Process parameters optimization for improving surface quality and manufacturing accuracy of binder jetting additive manufacturing process, Rapid Prototyping Journal, 22 (2016) 527-538.
- [11] S. Shrestha, G. Manogharan, Optimization of binder jetting using Taguchi method, Jom, 69 (2017) 491-497.
- [12] T. Do, P. Kwon, C.S. Shin, Process development toward full-density stainless steel parts with binder jetting printing, International Journal of Machine Tools and Manufacture, 121 (2017) 50-60.
- [13] N. Lecis, R. Beltrami, M. Mariani, Binder jetting 3D printing of 316 stainless steel: Influence of process parameters on microstructural and mechanical properties, Metallurgia Italiana, 113 (2021) 31-41.
- [14] N.B. Crane, Impact of part thickness and drying conditions on saturation limits in binder jet additive manufacturing, Additive Manufacturing, 33 (2020).
- [15] M. Vaezi, C.K. Chua, Effects of layer thickness and binder saturation level parameters on 3D printing process, The International Journal of Advanced Manufacturing Technology, 53 (2011) 275-284.

- [16] M. Zago, N.F.M. Lecis, M. Vedani, I. Cristofolini, Dimensional and geometrical precision of parts produced by binder jetting process as affected by the anisotropic shrinkage on sintering, Additive Manufacturing, 43 (2021).
- [17] B.J. Paudel, D. Conover, J.-K. Lee, A.C. To, A computational framework for modeling distortion during sintering of binder jet printed parts, Journal of Micromechanics and Molecular Physics, 6 (2021) 95-102.
- [18] K. Zhang, W. Zhang, R. Brune, E. Herderick, X. Zhang, J. Cornell, J. Forsmark, Numerical simulation and experimental measurement of pressureless sintering of stainless steel part printed by Binder Jetting Additive Manufacturing, Additive Manufacturing, 47 (2021) 102330.
- [19] S. Sadeghi Borujeni, A. Shad, K. Abburi Venkata, N. Gunther, V. Ploshikhin, Numerical simulation of shrinkage and deformation during sintering in metal binder jetting with experimental validation, Materials and Design, 216 (2022).
- [20] S. Sadeghi Borujeni, G.S. Saluja, V. Ploshikhin, Compensation of sintering deformation for components manufactured by metal binder jetting using numerical simulations, Rapid Prototyping Journal, 29 (2023) 612-625.
- [21] N.J. Salim, I. Arretche, K.H. Matlack, A process to spatially control the fraction of SS420 and bronze phases in binder jet infiltrated parts, Journal of Manufacturing Processes, 85 (2023) 612-622.
- [22] K.M. Rahman, A. Wei, H. Miyanaji, C.B. Williams, Impact of binder on part densification: Enhancing binder jetting part properties through the fabrication of shelled geometries, Additive Manufacturing, 62 (2023) 103377.
- [23] M. Li, G. Miao, W. Du, Z. Pei, C. Ma, Difference between powder bed density and green density for a free-flowing powder in binder jetting additive manufacturing, Journal of Manufacturing Processes, 84 (2022) 448-456.
- [24] E. Sachs, M. Cima, J. Cornie, D. Brancazio, J. Bredt, A. Curodeau, T. Fan, S. Khanuja, A. Lauder, J. Lee, Three-dimensional printing: the physics and implications of additive manufacturing, CIRP annals, 42 (1993) 257-260.
- [25] E. Stevens, S. Schloder, E. Bono, D. Schmidt, M. Chmielus, Density variation in binder jetting 3D-printed and sintered Ti-6Al-4V, Additive Manufacturing, 22 (2018) 746-752.
- [26] M. Denesuk, G. Smith, B. Zelinski, N. Kreidl, D.R. Uhlmann, Capillary penetration of liquid droplets into porous materials, Journal of colloid and interface science, 158 (1993) 114-120.
- [27] R.K. Holman, M.J. Cima, S.A. Uhland, E. Sachs, Spreading and infiltration of inkjet-printed polymer solution droplets on a porous substrate, Journal of colloid and interface science, 249 (2002) 432-440.
- [28] H.N. Emady, D. Kayrak-Talay, W.C. Schwerin, J.D. Litster, Granule formation mechanisms and morphology from single drop impact on powder beds, Powder Technology, 212 (2011) 69-79.
- [29] T. Nguyen, W. Shen, K. Hapgood, Drop penetration time in heterogeneous powder beds, Chemical Engineering Science, 64 (2009) 5210-5221.

- [30] J.O. Marston, S.T. Thoroddsen, W.K. Ng, R.B.H. Tan, Experimental study of liquid drop impact onto a powder surface, Powder Technology, 203 (2010) 223-236.
- [31] J.O. Marston, J.E. Sprittles, Y. Zhu, E.Q. Li, I.U. Vakarelski, S.T. Thoroddsen, Drop spreading and penetration into pre-wetted powders, Powder Technology, 239 (2013) 128-136.
- [32] H.N. Emady, D. Kayrak Talay, J.D. Litster, A regime map for granule formation by drop impact on powder beds, AIChE Journal, 59 (2013) 96-107.
- [33] K.P. Hapgood, T.H. Nguyen, S. Hauw, S.M. Iveson, W. Shen, Rewetting effects and droplet motion on partially wetted powder surfaces, AIChE Journal, 55 (2009) 1402-1415.
- [34] T. Fan, Droplet-powder impact interaction in three dimensional printing, in, Massachusetts Institute of Technology, 1996.
- [35] H. Miyanaji, S. Zhang, L. Yang, A new physics-based model for equilibrium saturation determination in binder jetting additive manufacturing process, International Journal of Machine Tools and Manufacture, 124 (2018) 1-11.
- [36] Y. Bai, C. Wall, H. Pham, A. Esker, C.B. Williams, Characterizing Binder–Powder Interaction in Binder Jetting Additive Manufacturing Via Sessile Drop Goniometry, Journal of Manufacturing Science and Engineering, 141 (2019).
- [37] H. Tan, Three-dimensional simulation of micrometer-sized droplet impact and penetration into the powder bed, Chemical Engineering Science, 153 (2016) 93-107.
- [38] S.L. Fuchs, P.M. Praegla, C.J. Cyron, W.A. Wall, C. Meier, A versatile SPH modeling framework for coupled microfluid-powder dynamics in additive manufacturing: binder jetting, material jetting, directed energy deposition and powder bed fusion, Engineering with Computers, 38 (2022) 4853-4877.
- [39] R. Sadeghi, M.S. Shadloo, M. Hopp-Hirschler, A. Hadjadj, U. Nieken, Three-dimensional lattice Boltzmann simulations of high density ratio two-phase flows in porous media, Computers & Mathematics with Applications, 75 (2018) 2445-2465.
- [40] H. Deng, Y. Huang, S. Wu, Y. Yang, Binder jetting additive manufacturing: Three-dimensional simulation of micro-meter droplet impact and penetration into powder bed, Journal of Manufacturing Processes, 74 (2022) 365-373.
- [41] J.J. Wagner, C. Fred Higgs, Computation of hydrodynamic and capillary phenomena in binder jet three-dimensional printing, Journal of Tribology, 143 (2021).
- [42] H. Tan, Absorption of millimeter-and micrometer-sized droplets on nylon powder, Experiments in Fluids, 63 (2022) 187.
- [43] T. Colton, N.B. Crane, Influence of droplet velocity, spacing, and inter-arrival time on line formation and saturation in binder jet additive manufacturing, Additive Manufacturing, 37 (2021).
- [44] N.D. Parab, J.E. Barnes, C. Zhao, R.W. Cunningham, K. Fezzaa, A.D. Rollett, T. Sun, Real time observation of binder jetting printing process using high-speed X-ray imaging, Scientific Reports, 9 (2019) 2499.

- [45] T. Colton, C. Inkley, A. Berry, N.B. Crane, Impact of inkjet printing parameters and environmental conditions on formation of 2D and 3D binder jetting geometries, Journal of Manufacturing Processes, 71 (2021) 187-196.
- [46] C.G. Inkley, J.E. Lawrence, N.B. Crane, Impact of controlled prewetting on part formation in binder jet additive manufacturing, Additive Manufacturing, 72 (2023) 103619.
- [47] H.J. O'Connor, A.N. Dickson, D.P. Dowling, Evaluation of the mechanical performance of polymer parts fabricated using a production scale multi jet fusion printing process, Additive Manufacturing, 22 (2018) 381-387.
- [48] A. Ellis, C. Noble, N. Hopkinson, High Speed sintering: Assessing the influence of print density on microstructure and mechanical properties of nylon parts. Addit Manufact 1: 48–51, in, 2014.
- [49] J.E. Lawrence, H.A.P. Vega, B. Stegman, C. Roberts, J. Spencer, C. James, M. Christensen, N. Crane, Construction of Open-Source Laboratory-Scale Binder Jetting System for High-Speed Synchrotron X-Ray Imaging, in: Solid Freeform Fabrication Symposium An Additive Manufacturing Conference Austin, TX, USA, 2022.
- [50] P.R. Baker, Three dimensional printing with fine metal powders, in, Massachusetts Institute of Technology, 1997.
- [51] R. Yang, R. Zou, A. Yu, Computer simulation of the packing of fine particles, Physical review E, 62 (2000) 3900.
- [52] C. Meier, R. Weissbach, J. Weinberg, W.A. Wall, A.J. Hart, Critical influences of particle size and adhesion on the powder layer uniformity in metal additive manufacturing, Journal of Materials Processing Technology, 266 (2019) 484-501.
- [53] Z. Yang, Y. Zhang, W. Yan, High-fidelity modeling of binder-powder interactions in binder jetting: Binder flow and powder dynamics, Acta Materialia, (2023) 119298.
- [54] K.P. Hapgood, J.D. Litster, S.R. Biggs, T. Howes, Drop penetration into porous powder beds, J Colloid Interface Sci, 253 (2002) 353-366.
- [55] N. Mitarai, F. Nori, Wet granular materials, Advances in physics, 55 (2006) 1-45.
- [56] R.M. German, Coordination number changes during powder densification, Powder Technology, 253 (2014) 368-376.
- [57] L. Marchetti, P. Mellin, C. Neil Hulme, Negative impact of humidity on the flowability of steel powders, Particulate Science and Technology, 40 (2022) 722-736.
- [58] E.W. Washburn, The Dynamics of Capillary Flow, Physical Review, 17 (1921) 273-283.
- [59] H. Katsuragi, Length and time scales of a liquid drop impact and penetration into a granular layer, Journal of fluid mechanics, 675 (2011) 552-573.